



High-Rate Li⁺ Storage Capacity of Surfactant-Templated Graphene-TiO₂ Nanocomposites

Andrew G. Hsieh,^{a,c} Christian Punckt,^{a,b,d} and Ilhan A. Aksay^{a,z}

^aDepartment of Chemical and Biological Engineering, Princeton University, Princeton, New Jersey 08544, USA

^bVorbeck Princeton Research Center, Vorbeck Materials Corp., Monmouth Junction, New Jersey 08852, USA

Graphene-TiO₂ nanocomposites are a promising anode material for Li-ion batteries due to their good high-rate capacity, inherent safety, and mechanical and chemical robustness. However, despite a large number of scientific reports on the material, the mechanism of the enhanced high-rate Li⁺ storage capacity that results from the addition of graphene to TiO₂ – typically attributed to improved electrical conductivity – is still not well understood. In this work, we focus on optimizing the processing of surfactant-templated graphene-TiO₂ hybrid nanocomposites. Towards this end, we examine the influence of various processing parameters, in particular the surfactant-mediated colloidal dispersion of graphene, on the material properties and electrochemical performance of graphene-TiO₂. We investigate the influence of electrode mass loading on Li⁺ storage capacity, focusing mainly on high-rate performance. Furthermore, we demonstrate an approach for estimating power loss during charge/discharge cycling, which offers a succinct method for characterizing the high-rate performance of Li-ion battery electrodes.

© The Author(s) 2015. Published by ECS. This is an open access article distributed under the terms of the Creative Commons Attribution Non-Commercial No Derivatives 4.0 License (CC BY-NC-ND, <http://creativecommons.org/licenses/by-nc-nd/4.0/>), which permits non-commercial reuse, distribution, and reproduction in any medium, provided the original work is not changed in any way and is properly cited. For permission for commercial reuse, please email: oa@electrochem.org. [DOI: 10.1149/2.0481508jes] All rights reserved.

Manuscript submitted February 2, 2015; revised manuscript received April 17, 2015. Published May 23, 2015.

Metal oxides have been studied extensively as anode materials for Li-ion batteries due to their comparably high Li-insertion/extraction potentials,^{1,2} which make them inherently safe from Li-electroplating and dendrite formation, thus preventing membrane perforation and cell shorting even at high lithiation currents. Additionally, good mechanical and chemical stability during operation enables long cycling lifetimes.²⁻⁴ However, large oxide particles are restricted to slow charge/discharge rates (< C/5, meaning charge/discharge times > 5 h) because of low diffusion rates of Li⁺⁵⁻⁸ and poor electrical conductivity in oxides. Much work has therefore been done to address these limitations, with significant attention placed on titanium dioxide (TiO₂)⁹⁻¹² because it is abundant and chemically inert, and the availability of simple processes for producing nanostructured (i.e., nano-sized or nano-porous) TiO₂ make it attractive for large-scale use.

Nanostructuring of TiO₂ improves Li⁺ transport mainly by decreasing the length of Li⁺ diffusion pathways through the oxide during lithiation/delithiation.^{8,13-15} In addition, the diffusivity of Li⁺ in TiO₂ can be enhanced by using surfactant templates to orient the growth of the oxide.¹⁶⁻¹⁸ To improve electron transport in TiO₂ electrodes, on the other hand, conductive coatings¹⁹⁻²² or additives²³ are commonly used. An especially effective approach is the formation of hybrid nanocomposite electrodes,^{15,24-27} in which nanostructured TiO₂ is intimately interconnected with a nanostructured conductive additive. Functionalized graphene sheets (FGSs)^{28,29} are attractive as conductive additives for such hybrid electrodes due to their good electrical properties.³⁰ Additionally, FGSs are ideal substrates for the surfactant-templated growth of oriented TiO₂ nanocrystals, as the high surface area³¹ and flexibility³² of FGSs enable a high degree of interfacial contact with the oxide, promoting efficient electron transport between them.

In 2009, Wang et al. demonstrated the effectiveness of this approach,²⁹ producing hybrid nanocomposites of FGSs and TiO₂ nanocrystals via an aqueous, surfactant-mediated process in which the anionic surfactant sodium dodecyl sulfate (SDS) acted both as a dispersant for FGSs³³ and as a template for TiO₂ growth.³⁴⁻³⁶ The FGS-TiO₂ hybrid nanocomposites that resulted from this scalable, one-step process exhibited remarkably greater high-rate Li⁺ storage capacities than TiO₂ nanoparticles alone. While it is clear that the

electrical conductivity imparted by FGSs was a major factor in the enhanced high-rate performance, it is still unknown if template-assisted nucleation of TiO₂ on FGSs also affects the properties of TiO₂ as well as the transport of Li⁺ in the system. Most importantly, systematic investigation and characterization of the influence of processing parameters on the material properties and high-rate Li⁺ storage capacity of FGS-TiO₂ electrodes are still needed in order to optimize the process. Of particular interest is the SDS concentration, [SDS], as it directly influences the adsorption of SDS on FGSs³⁷ and in turn the aggregation/deaggregation of FGSs during processing,³³ and also because SDS micelles template the growth of TiO₂.³⁴⁻³⁶ At [SDS] above the critical micelle concentration (cmc), as is the case in the Wang et al. study,²⁷ micelles are present in bulk solution as well as on FGSs;³⁷ at [SDS] just below the cmc, however, micelles will only be present on FGSs.³⁷ As such, the [SDS] used in the processing of FGS-TiO₂ will strongly influence where TiO₂ growth occurs and how intimately interconnected FGSs and TiO₂ will be, which will significantly affect the Li⁺ storage performance of the nanocomposites. Furthermore, as the practical energy density of the system depends, in part, on the fraction of active mass present,³⁸ it is also necessary to investigate the effect of electrode mass loading, i.e., the amount of active material per unit electrode area, on the Li⁺ storage performance of FGS-TiO₂ electrodes.

In this study, we optimize the processing of FGS-TiO₂ by systematically examining the impact of processing parameters on both the material properties and Li⁺ storage capacity of the hybrid nanocomposites, with a specific focus on the surfactant concentration. We study the influence of electrode mass loading on Li⁺ storage capacity, focusing mainly on high-rate performance (at 3.4 A/g or ~20C based on TiO₂), and demonstrate an approach for estimating the power loss during charge/discharge cycling in order to characterize and compare the high-rate performance of different FGS-TiO₂ electrodes. Our results indicate that changes in the morphology, resistivity, and porosity of FGS-TiO₂ electrodes influence their high-rate Li⁺ storage capacity. Through an optimization of the processing parameters to maximize the electrochemical contribution of TiO₂ that is in intimate contact with FGSs, we achieve further improvements over the results reported by Wang et al.²⁷ in terms of high-rate performance, particularly at high mass loadings.

Methods

Processing of FGSs.— Graphite oxide (GO) was prepared according to the method of Tour et al.³⁹ About 100 mg of the GO was placed

^cPresent Address: Department of Mechanical and Aerospace Engineering, Princeton University, Princeton, New Jersey.

^dPresent Address: Institute of Nanotechnology, Karlsruhe Institute of Technology, Karlsruhe, Germany.

^zE-mail: iaksay@princeton.edu

Table I. Summary of the parameters used to process the FGS-TiO₂ samples.

Sample	Final [TiCl ₃] (mM)	T _{rxn} (°C)	t _{rxn} (h)	0.1 M SDS (mL)	Final [SDS] (mM)	3 wt% H ₂ O ₂ (mL)	wt% TiO ₂
P-6.5	37.5	90	16	13	6.5	2.1	93
M-6.5	12.5	50	0.5	13	6.5	0.7	85
M-0.65	12.5	50	0.5	1.3	0.65	0.7	80
M-0	12.5	50	0.5	0	0	0.7	81

at the bottom of a fused silica tube (Technical Glass Products) and dried overnight under flowing nitrogen. The tube was evacuated and then purged with ultra-high purity argon (Grade 5.5, Air Products) three times. The tube was evacuated once more and, while still under vacuum, thermal exfoliation and simultaneous reduction of GO were carried out by placing the tube in a three-zone tube furnace (Lindberg/Blue M, SPX Thermal Product Solutions), which was set to a temperature of 1100 °C, for 60 s. The molar carbon-to-oxygen ratio (C/O) of the resulting FGSs was ~21, measured with energy dispersive X-ray spectroscopy (EDS, INCA x-act, Oxford Instruments, attached to a Vega 1 scanning electron microscope, Tescan USA).

Processing and characterization of FGS-TiO₂.— In the processing of FGS-TiO₂ samples, one of four sets of reaction parameters was used as summarized in Table I. The parameters for the P-6.5 sample were identical to those used in the Wang et al. study.²⁷ For the other three samples, the TiCl₃ precursor concentration ([TiCl₃]), reaction temperature (T_{rxn}), and reaction time (t_{rxn}) were reduced, which act to decrease the extent of TiO₂ formation.⁴⁰ Between the M-6.5, M-0.65, and M-0 samples (collectively, the M-samples), the [SDS] was altered, which influences the adsorption of SDS onto FGSs³⁷ and thus the dispersion behavior of FGSs,³³ as well as the nucleation and growth of TiO₂.^{35,41} At the ionic strengths of the aqueous reaction mixtures, the cmc for SDS is ~0.8–1 mM.^{42,43} Thus, with these three samples, we cover a wide range from no SDS (0 mM), to an [SDS] slightly below the cmc (0.65 mM) yielding micelles on the graphene sheets, to an [SDS] significantly above the cmc (6.5 mM) yielding micelles both on the graphene sheets and the bulk solution.

In a typical reaction, 10 mg of FGSs were mixed with the required volume of a 0.1 M SDS stock solution and diluted to 50 mL with DI water. The mixture was sonicated at ~300 W (VCX 750 ultrasonic processor unit, Sonics & Materials, Inc.) for 30 min while cooling in an ice bath. A 50 mL portion of aqueous TiCl₃, prepared at the appropriate concentration from a stock TiCl₃ solution (≥12% with 5% HCl, Sigma Aldrich), was added to the SDS-FGS dispersion while stirring, followed by 12.5 mL of a 0.6 M Na₂SO₄ aqueous solution. A sufficient amount of HCl and DI water was added to adjust the pH to 0.8 and volume to 200 mL, and the suspension was sonicated again for ~30 s.

The state of FGS aggregation in the suspension was determined with optical microscopy imaging (Axioplan 2, Carl Zeiss Microscopy) using a water immersion objective (C-Apochromat 63x/1.2 W Korr, Carl Zeiss Microscopy). The suspension was then transferred to a jacketed beaker, which was connected to a constant temperature bath (F25-MV refrigerated-heating circulator, Julabo USA, Inc.) set to the desired reaction temperature, the aliquot of 3 wt% H₂O₂ was added drop-wise, and stirred for the desired reaction time. The reaction was then quenched with 200 mL of chilled DI water, and optical imaging was carried out to determine the morphology of the FGS-TiO₂. The suspension was then passed through a membrane with a nominal pore size of 0.22 μm using a vacuum filter to collect the FGS-TiO₂, and three 200 mL aliquots of DI water were then passed through sequentially to wash the product.

The collected material was placed in a vacuum oven set to ~80 °C to dry overnight, then calcined in air at 400 °C for 2 h. Thermogravimetric analysis (TGA, Q50 Analyzer, TA Instruments) was used to determine the mass fraction of TiO₂ in the resulting ma-

terial by heating the sample to 1000 °C at a rate of 20 °C/min in air. X-ray diffraction (XRD) spectra of the FGS-TiO₂ samples were gathered using Cu K_α radiation (Miniflex II, Rigaku Corporation).

Electrochemical analysis and characterization of FGS-TiO₂ slurries.— Following standard electrode preparation procedure,^{44,45} electrode slurry mixtures were made with the FGS-TiO₂ active material, Super P carbon black (Timcal Graphite & Carbon) as a conductive additive to ensure electrical pathways between active particles and the current collector, and poly(vinylidene fluoride) (PVDF) binder for mechanical robustness at a mass ratio of 80:10:10. In a vial, we combined the FGS-TiO₂ and Super P with an appropriate amount of PVDF that had been dissolved at 2.5 wt% in N-methyl-pyrrolidone (NMP). The slurry was then homogenized (X120 handheld homogenizer drive with T6 shaft and generator, CAT Scientific) for several minutes to ensure thorough mixing.

To process the electrodes, a sheet of aluminum foil was wiped clean with an isopropanol-soaked fiber cloth and pressed flat onto a glass sheet. The slurry was placed onto the foil, and a stainless steel coating applicator (PA-5355 multiple clearance square applicator, BYK Additives & Instruments) was used to cast films with different thicknesses, enabling various electrode mass loadings to be obtained. After the films were dried overnight, they were not calendared or otherwise pressed prior to cell assembly. Circular electrodes were punched out from each of the films and placed in a vacuum oven set to ~90 °C for at least 1 h to allow for further drying. The electrodes were imaged with a field emission scanning electron microscope (SEM, Quanta 200 FEG, FEI Company) at 15 kV acceleration voltage using both the secondary and backscattered electron detectors.

For electrochemical testing, coin cells (type CR2032, MTI Corporation) were assembled in an argon-filled glove box (PureLab HE Glovebox System, Innovative Technology, Inc.), using the dried FGS-TiO₂ electrodes as the working electrode (WE) and Li foil as the reference and counter electrode, separated from each other by a polypropylene membrane (type 3501, Celgard, LLC). The electrolyte was a 1 M solution of LiPF₆ in ethylene carbonate/dimethyl carbonate (1:1 volume ratio). The coin cells were compressed with ~2.2 kN (~6.9 MPa or 1000 psi of stack pressure for a 2032 cell size) for several seconds during crimping.

For each sample in Table I, cells were made with electrodes at a range of mass loadings. The cells were cycled under galvanostatic (constant current) control at mass-specific currents $i = 0.17, 0.34, 0.67, 1.7,$ and 3.4 A/g between voltage limits of 1 and 3 V vs. Li/Li⁺ (BT-2000 test station, Arbin Instruments; VSP and SP-300 potentiostats, Bio-Logic USA) to measure their mass-specific Li⁺ storage capacities. The capacities over a final set of cycles at 0.17 A/g were measured to ensure that the cells had not catastrophically failed during testing. The mass-specific currents and Li⁺ storage capacities were calculated based on the mass fraction (wt%) of TiO₂ as measured by TGA (Table I). Our sign convention regarding charge and discharge currents is the following: During cycling, when i is positive, the WE potential increases as Li⁺ migrates out of the FGS-TiO₂ electrode; this is referred to as the de-lithiation step. Conversely, when i is negative, the WE potential decreases as Li⁺ migrates into the electrode; this is referred to as the lithiation step.

The surface areas of the FGS-TiO₂ electrodes were determined from nitrogen adsorption isotherms (Gemini V, Micrometrics Instruments Corporation) by the Brunauer, Emmett, and Teller (BET) method.⁴⁶ A pore size analysis of the FGS-TiO₂ electrodes was carried out using nitrogen condensation analysis, and the pore size distributions and total pore volumes for each sample were calculated from the evaporation/desorption isotherms following an approach described elsewhere by Dollimore and Heal.⁴⁷

To measure the differences in the electrical properties between samples, the same FGS-TiO₂ slurries used for electrochemical testing were cast onto sheets of poly(ethylene terephthalate) (PET). After drying overnight in air, the sheet resistance R_s of each sample was measured with a four-point probe method: four strips of copper tape were applied to the same side of a glass slide, which was then pressed,

copper-side down, onto rectangular sections of the FGS-TiO₂ coated PET. Using a potentiostat (SP-150, Bio-Logic USA), the potential difference between the two inner pieces of copper tape was measured while a constant current of 5 μ A was applied to the two outer pieces. The potential drop V and applied current I were used to calculate R_s of each sample using the formula $R_s = \frac{V}{I} \cdot \frac{w}{\ell}$, where w and ℓ are the width of the sample and the distance between the two points where V was measured, respectively. The mass-specific resistivity of the sample $\hat{\rho}$ was then calculated by multiplying R_s by the mass loading of the FGS-TiO₂ on PET.

Results and Discussion

To demonstrate the impact of processing parameters on the electrochemical performance of FGS-TiO₂, we first show the results from standard galvanostatic cycling of each sample listed in Table I, using electrodes with various mass loadings. These data are used to show overall trends in Li⁺ storage capacity as well as to determine the power loss during cycling. We then present results from the characterization of each sample throughout the nanocomposite processing and electrode fabrication processes, which we correlate with the electrochemical data.

Galvanostatic lithiation/de-lithiation cycling tests.— The voltage-capacity (V - Q) curves obtained during galvanostatic cycling of a representative FGS-TiO₂ electrode are shown in Figure 1a for the range of i that was tested. As the WE is lithiated ($i < 0$) and de-lithiated ($i > 0$), we observe the well-known pair of voltage plateaus that occur on ei-

ther side of the equilibrium potential, V_{eq} , for the reversible insertion of Li⁺ into anatase TiO₂ (~ 1.85 V vs. Li/Li⁺).^{9,48} The plateaus are shifted from V_{eq} due to the various dissipative processes that occur during cycling, which make it necessary to apply an overpotential in order to drive the current. Increasing the magnitude of i , i.e., the rate at which the cell is lithiated or de-lithiated, causes the voltage plateaus to shift further from V_{eq} . This is expected, as the dissipative losses are increasing functions of i , i.e., greater overpotentials are necessary to drive a larger current. Values of the capacity measured during each step, Q_{step} , are plotted in Figure 1b for different values of i for two representative cells with different mass loadings, i.e., different amounts of active material per unit electrode area. As expected from the V - Q curves in Figure 1a, Q_{step} decreases as the magnitude of i increases. Furthermore, at each value of i , the cell with the higher electrode mass loading has a lower Q_{step} . This is due to increased transport losses as e⁻ and Li⁺ need to diffuse along greater distances through the electrode and the electrolyte, respectively, as well as to the overall increase in current density (i.e., current per unit electrode area), which causes the dissipative losses to further increase in magnitude.

The cycling results for the samples listed in Table I are summarized in Figure 2; for each cell, we plot Q_{step} from the last cycle at each i as a function of the electrode mass loading. A line is drawn through the data for every value of i as a guide for the eye. All the samples show qualitatively similar trends: (i) At a given rate, Q_{step} decreases as mass loading increases, and (ii) at a given mass loading, Q_{step} decreases as i increases. Additionally, for reasons that are discussed in a later section, in all the samples except for M-6.5, the drop in Q_{step} with increasing mass loading is steeper at higher i , and the decrease in Q_{step} as i increases is stronger at higher loadings.

To demonstrate the quantitative differences between the samples, we focus on the Q_{step} measured at the lowest and highest i tested (0.17 and 3.4 A/g, respectively), as summarized in Figure 3: At $i = 0.17$ A/g, Q_{step} for P-6.5 is lower than that of the M-samples for mass loadings < 1 mg TiO₂/cm²; however, at mass loadings > 1.5 mg TiO₂/cm², the difference in capacity between P-6.5 and the M-samples is smaller and the Q_{step} of P-6.5 is comparable to that of M-0. At $i = 3.4$ A/g, a larger variability in the dependence of Q_{step} on mass loading is observed: For loadings < 1 mg TiO₂/cm², Q_{step} for M-0.65 and M-0 are greater than Q_{step} for the other two samples. In contrast, at loadings > 1.5 mg TiO₂/cm², M-6.5 has the largest Q_{step} while P-6.5 and M-0.65 have the lowest.

From these data, it is clear that the parameters used to process the FGS-TiO₂ nanocomposites have a significant impact on electrochemical performance, evident from the differences between the samples in how Q_{step} changes with i as well as electrode mass loading. As noted above, for a given sample, higher current densities lead to larger resistive losses (from e⁻ transport in the electrode material and Li⁺ transport in the electrolyte) and kinetic losses (from both the intrinsic reaction kinetics and the effective accessible-surface-area-dependent kinetics). Thus, as current density is the product of i with mass loading, Q_{step} depends most strongly on electrode mass loading at the highest lithiation/de-lithiation rates. Consequently, the influence of FGS-TiO₂ reaction parameters on electrochemical performance is most apparent at the highest i and mass loadings, which is also the most technologically-interesting regime of high power density. In order to succinctly quantify and characterize the high-rate performance of the FGS-TiO₂ samples at different electrode mass loadings, in the following subsection we describe an approach to estimate the power loss P_{loss} during lithiation and de-lithiation.

Estimating P_{loss} for lithiation and de-lithiation.— The power P at which a half-cell is operated vs. lithium metal can be expressed as:^{49,50}

$$P = i \cdot [V_{eq} - \Delta V_{loss}] \quad [1]$$

where ΔV_{loss} represents the sum of all voltage drops (overpotential) occurring across the cell. Note that for a full cell, the cell voltage (i.e., the difference in the equilibrium potentials of the anode and cathode) would be used instead of V_{eq} . The magnitude of P_{loss} , which

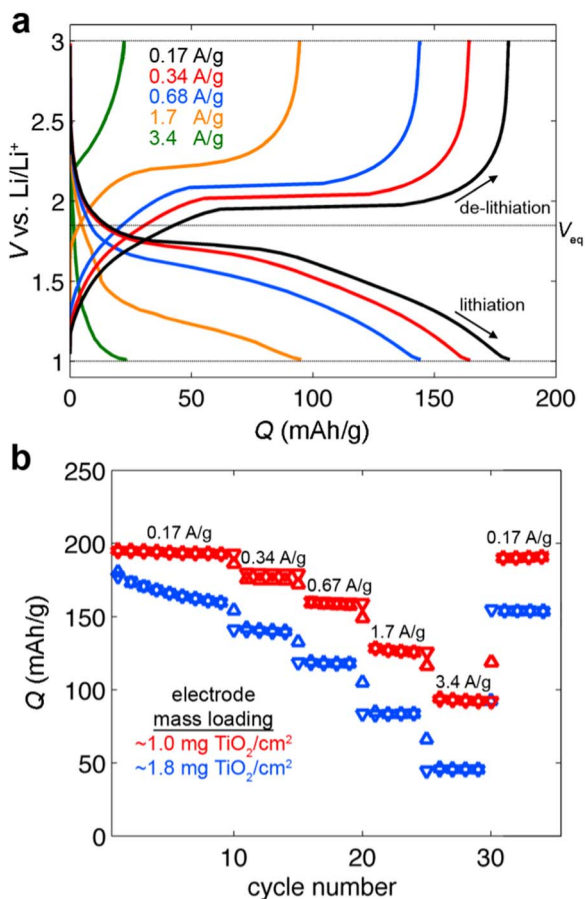


Figure 1. (a) Voltage vs. capacity (V - Q) curves measured during the galvanostatic cycling of a representative FGS-TiO₂ electrode, as a function of the lithiation/de-lithiation current, i . (b) The capacity, Q , for each cycle measured at the various i tested; data is shown for two representative cells with different electrode mass loadings.

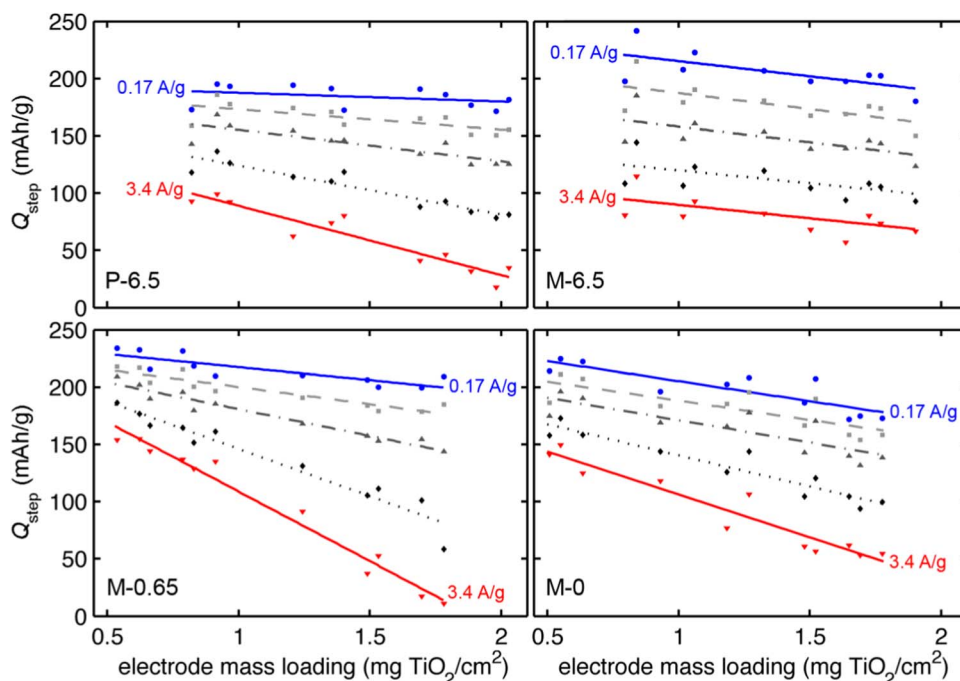


Figure 2. Q_{step} of FGS-TiO₂ electrodes from the (top left) P-6.5, (top right) M-6.5, (bottom left) M-0.65, and (bottom right) M-0 reactions (Table I). Q_{step} was measured at $i = 0.17$ A/g (blue solid line, circles), 0.34 A/g (light gray dashed line, squares), 0.67 A/g (medium gray dash-dotted line, up triangles), 1.7 A/g (black dotted line, diamonds), and 3.4 A/g (red solid line, down triangles). The data are displayed as a function of electrode mass loading; i and Q_{step} were calculated with respect to the wt% TiO₂ in each sample (Table I).

is independent of the choice of counter electrode, can be expressed as:

$$P_{\text{loss}} = i \cdot \Delta V_{\text{loss}} \quad [2]$$

To determine ΔV_{loss} for our data, we first plot the differential capacity $\frac{dQ}{dV}$ vs. V as shown for a representative cell in Figure 4a. ΔV_{loss} can be estimated from these data as follows: The peaks in $\frac{dQ}{dV}$ correspond to the V - Q plateaus in Figure 1a, and their positions during the lithiation ($\frac{dQ}{dV} < 0$) and de-lithiation ($\frac{dQ}{dV} > 0$) steps are indicated as $V_{\text{pk,lith}}$ and $V_{\text{pk,delith}}$, respectively. As the shifts in $V_{\text{pk,lith}}$ and $V_{\text{pk,delith}}$ ($\Delta V_{\text{pk,lith}} = |V_{\text{pk,lith}} - V_{\text{eq}}|$ and $\Delta V_{\text{pk,delith}} = |V_{\text{pk,delith}} - V_{\text{eq}}|$, respectively) are a result of the dissipative losses experienced by the cell during cycling, their magnitudes increase with i . As shown for a representative step in the inset of Figure 4a, both ΔV_{lith} and ΔV_{delith} display a power-law dependence on i . For a given step, then, the power-law expression for ΔV_{lith} or ΔV_{delith} (Fig. 4a inset) can be substituted into Equation 2 for ΔV_{loss} , which allows P_{loss} to be calculated as a function of i .

With this approach, for each FGS-TiO₂ sample, we calculate and plot P_{loss} as a function of electrode mass loading at the lowest and

highest specific currents that were tested ($i = 0.17$ and 3.4 A/g) for both the lithiation ($P_{\text{loss,lith}}$, Fig. 4b) and de-lithiation ($P_{\text{loss,delith}}$, Fig. 4c) steps. Lines are drawn through the data for each sample to guide the eye. At $i = 0.17$ A/g, the $P_{\text{loss,lith}}$ curves all lie nearly on top of one another; the M-0.65 curve has a slightly larger slope, and it deviates to larger $P_{\text{loss,lith}}$ values than the others at higher mass loadings; in contrast, the $P_{\text{loss,delith}}$ curves are offset from one other and appear nearly parallel, except for the M-6.5 curve, which has a smaller slope. At $i = 3.4$ A/g, the power loss during both lithiation and de-lithiation is two orders of magnitude greater than at 0.17 A/g. At low mass loadings (< 1 mg TiO₂/cm²), the differences in $P_{\text{loss,lith}}$ and $P_{\text{loss,delith}}$ between the different samples are insignificant, with the exception of $P_{\text{loss,delith}}$ for M-0.65 and M-0 being slightly lower than the others. At mass loadings > 1.5 mg TiO₂/cm², on the other hand, $P_{\text{loss,lith}}$ and $P_{\text{loss,delith}}$ for M-0.65 are distinctly greater than the others while for M-6.5 they are clearly the lowest. Between the four processing routes, we observe that in general, a larger increase in P_{loss} with mass loading is correlated with larger decreases in Q_{step} at the same i (Fig. 2). This validates our approach for characterizing the high-rate performance of the cells by estimating $P_{\text{loss,lith}}$ and $P_{\text{loss,delith}}$.

Based on these data, there is clearly a link between the parameters used to process the FGS-TiO₂ samples and their high-rate Li⁺ storage capacities. This can be due to differences in the amount of energy dissipated within the cells during (i) the insertion/extraction of Li⁺ into/from TiO₂, (ii) the transport of e⁻ and Li⁺ in FGS-TiO₂, and/or (iii) the transport of Li⁺ in the electrolyte. To understand the origins of the observed differences in the high rate Li⁺ storage capacity of FGS-TiO₂, in the following subsection we employ various material characterization techniques and attempt to correlate material properties with the observed electrochemical performance. In doing so, we aim to identify correlations between the processing parameters, material properties, and ultimately high-rate Li⁺ storage capacities of the FGS-TiO₂ electrodes.

Characterization of FGS-TiO₂ nanocomposites.— Representative optical microscopy images of the reaction mixtures were taken at two points in time: first after the reaction mixtures had been prepared

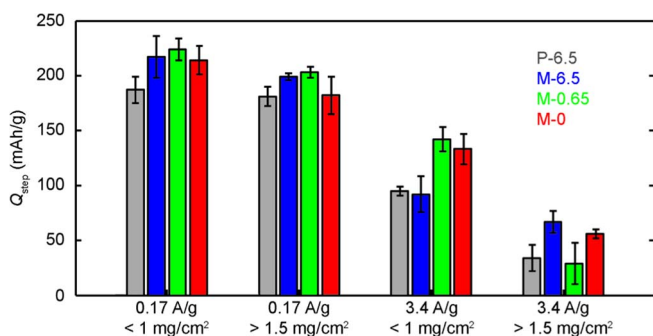


Figure 3. Bar chart summarizing the galvanostatic cycling data from Figure 2, emphasizing the difference between the FGS-TiO₂ samples with regards to the dependence of Q_{step} on electrode mass loading and i .

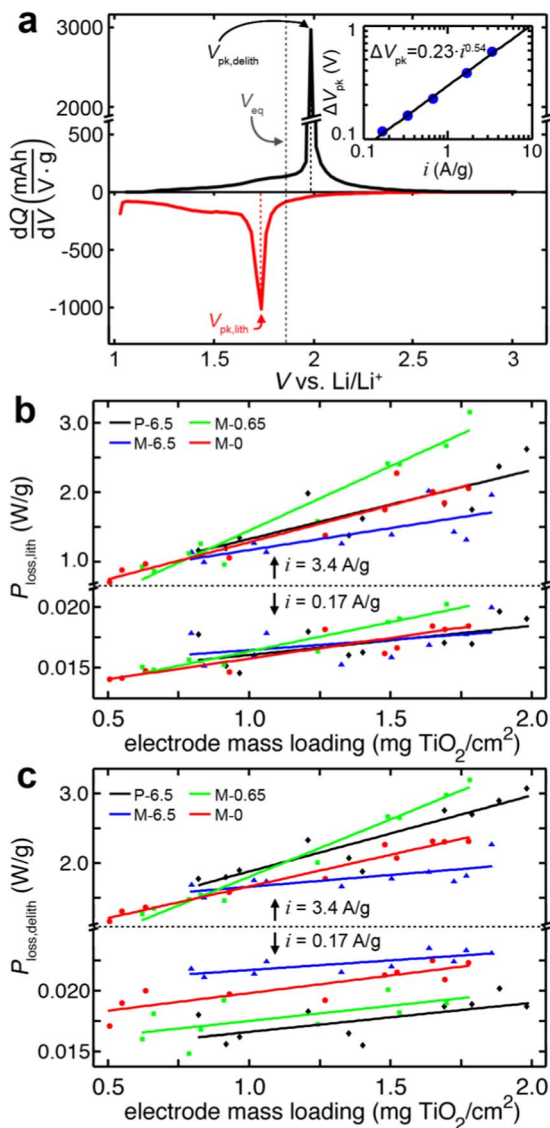


Figure 4. (a) Plot of $\frac{dQ}{dV}$ vs. V for a representative cycle, showing the lithiation (red) and de-lithiation (black) steps; the indicated potentials are described in the text. Inset: representative example of the power-law dependence of the $\frac{dQ}{dV}$ peak shift (ΔV_{pk}) on i . (b, c) The power lost to dissipation during lithiation, $P_{loss,lith}$, and de-lithiation, $P_{loss,delith}$, of the FGS-TiO₂ samples, as a function of electrode mass loading, at $i = 0.17$ and 3.4 A/g.

(but prior to heating, Fig. 5a), and again after the reaction mixtures had been quenched following the defined reaction times (Fig. 5b). Before heating the reaction mixtures, in the P-6.5 and M-6.5 samples, the FGSs (which show up as dark structures in optical images) are well dispersed but appear to be surrounded by lighter structures. As the [SDS] for these two samples (6.5 mM) is above the cmc for SDS at the ionic strengths of the reaction mixtures,^{42,43} the lighter structures are likely TiO₂ particles nucleated by bulk SDS micelles or by homogeneous nucleation in the solution. Conversely, in the M-0.65 and M-0 samples, the FGSs appear aggregated into branched and compact structures, respectively, and no TiO₂ particles appear to have nucleated in the bulk (as the [SDS] is below the cmc). After quenching the reactions, the FGSs in the P-6.5 and M-6.5 samples still appear to be dispersed and surrounded by a cloud of TiO₂ particles. The structures observed in the M-0.65 and M-0 samples appear to have retained their respective branched and more compact morphologies that were observed prior to the reaction.

After the samples were collected, dried, and calcined, their XRD spectra were gathered and are presented in Figure 5c. All four spectra indicate the presence of anatase TiO₂. No major differences in the widths of the main diffraction peaks are observed, indicating that the primary TiO₂ crystallites are similar in size between samples.

SEM images of the FGS-TiO₂ electrodes, taken after the slurries were cast and dried, are shown in Figure 6a; also indicated are the surface areas of the electrodes, as measured from nitrogen adsorption. The P-6.5 electrode contains many bright 1-2 μm -sized structures, while in the M-6.5 electrode these structures are 0.5-1 μm in size. The M-0.65 electrode contains bright structures that are 3-5 μm in size, and the M-0 electrode contains similar structures that are 1-2 μm in size. Cross-sectional SEM images of the electrodes are presented in Figure S1, and show that within each electrode the distribution of larger and smaller structures is even across the film thickness, indicating that no significant sedimentation occurred during drying. All the samples also contain darker, highly-textured regions which are the carbon black additive and polymer binder.⁵¹ Considering the optical images and XRD spectra (Fig. 5), as the [SDS] is above the cmc during processing of P-6.5 and M-6.5, the brighter structures observed in the corresponding SEM images are likely aggregates of TiO₂ particles that were nucleated by bulk micelles as well as embedded FGS-TiO₂ nanocomposites in which TiO₂ was templated on the FGSs by surface micelles through the self-assembly process described by Wang et al.²⁷ For the M-0.65 sample, as [SDS] was slightly below the cmc during processing and thus only surface micelles were present in the system,³⁷ the brighter structures observed in the corresponding SEM image are likely compact agglomerates of FGS-TiO₂ in which the TiO₂ was templated on FGSs by surface micelles again by the self-assembly process.²⁷ For the M-0 sample, the brighter structures observed in the corresponding SEM image are likely also compact agglomerates of FGS-TiO₂ (the presence of TiO₂ was confirmed by XRD), however the absence of SDS implies that the TiO₂ in this sample was not templated but rather had heterogeneously nucleated on aggregates of FGSs. Taken together, the optical and SEM images show that, as bulk-micelle-nucleated TiO₂ are present in the P-6.5 sample, they must have also been present in the original reported by Wang et al.²⁷

The incremental pore volume ($\frac{dV_p}{dr_p}$) of each of the four samples is plotted as a function of pore width r_p in Figure 6b; the inset shows the cumulative pore volume V_p as a function of (decreasing) r_p . All the samples have a peak in $\frac{dV_p}{dr_p}$ at ~ 2 nm. M-0.65 has the highest population of 2-nm pores and M-6.5 has the lowest. The values of V_p measured for the M-0.65 and M-0 samples are about twice the V_p values for M-6.5 and P-6.5. As the effective solid densities of the samples are similar (~ 3.1 – 3.3 g/cm³, as calculated from the respective densities and wt% of the individual electrode components), higher pore volumes correlate with higher electrode porosities. It should be noted, however, that the dried electrode film thicknesses are proportional to the slurry casting thickness and are independent of the FGS-TiO₂ processing parameters (see Table S2 and Figure S2). This suggests that despite the significant differences in microporosity as detected by nitrogen adsorption, the electrode films likely show similar porosity on larger length scales that are not measured by nitrogen adsorption.

From these results, it is clear that changes to the processing parameters between the FGS-TiO₂ samples affect their structure significantly. We will now discuss how this, in turn, influences the degree to which energy is dissipated (and power is lost) during galvanostatic cycling, which ultimately impacts the Li⁺ storage capacities of the electrodes. As the differences in $P_{loss,lith}$ and $P_{loss,delith}$ between the samples are most prominent at $i = 3.4$ A/g (Fig. 4b, 4c), in the following analysis we focus on the influence of processing parameters on the high-rate Li⁺ storage performance of FGS-TiO₂.

Electronic conductivity.—To assess the electronic properties of the electrodes, the sample slurries were cast onto PET and their mass-loading specific resistivities, $\hat{\rho}$, are presented in Figure 6c. For comparison, $\hat{\rho}$ of a slurry made from commercial anatase TiO₂

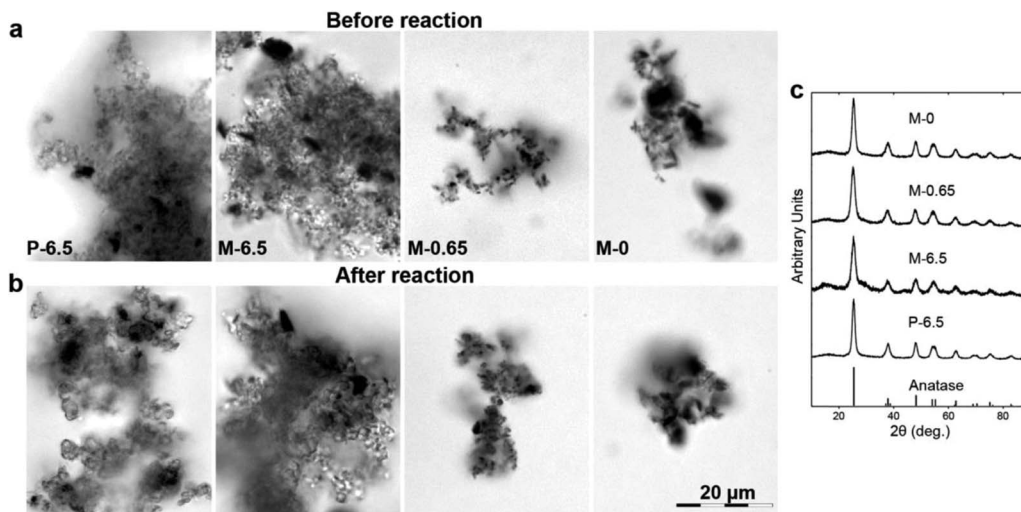


Figure 5. Optical images of the FGS-TiO₂ reaction mixtures, taken (a) just before the reactions were started (i.e., before heating) and (b) just after the reactions were quenched. (c) XRD spectra of the samples after they were dried and calcined.

(25 nm nominal particle size) was also measured. All the FGS-TiO₂ samples are more conductive than the commercial TiO₂. Furthermore, the values of $\hat{\rho}$ measured from the M-samples are the same, within error, and are lower than $\hat{\rho}$ for the P-6.5 sample.

The decrease in $\hat{\rho}$ between the TiO₂ and the FGS-TiO₂ samples reflects the improved e⁻ transport that results from the incorporation of FGSs, and is likely a major contributor to the enhanced Li⁺ storage capacity of FGS-TiO₂ compared to TiO₂.²⁷ From P-6.5 to M-6.5, the reduction in [TiCl₃], T_{rxn} , and t_{rxn} results in smaller bulk-micelle nucleated TiO₂ particles, as observed in the optical and SEM images (Figs. 5b and 6a, respectively), as well as a higher FGS content (Table I). The corresponding decrease in $\hat{\rho}$ (Fig. 6c) reflects a similar improvement in the e⁻ transport in the electrode and better “utilization” of TiO₂ during cycling; therefore, the decrease in $\hat{\rho}$ is likely to be a major contributor to the differences in high-rate performance between P-6.5 and M-6.5. Interestingly, though, while different concentrations

of SDS were used to process the M-samples, their electrical properties are similar as their $\hat{\rho}$ are all within error. Nonetheless, we have observed that the M-samples achieve very different values of Q_{step} at high-rates (Figs. 2 and 3). This implies that the differences in electrochemical performance between the M-samples are most likely ionic in nature.

Li⁺ transport.—As all the samples contain anatase TiO₂ with similar primary crystallite sizes, the intrinsic surface-area specific reaction kinetics for Li⁺ insertion/extraction are most likely identical. Instead, differences in Li⁺ transport (either within the FGS-TiO₂ or in the electrolyte) or in the effective kinetics (due to different electrolyte-accessible surface areas) are likely the major factors influencing the high-rate Li⁺ storage performance of the M-samples.

For lower mass loading (i.e., thinner) electrodes, porosity and other morphological effects will have less of an impact on electrochemical performance than for higher mass loading electrodes.^{52,53} Thus, in

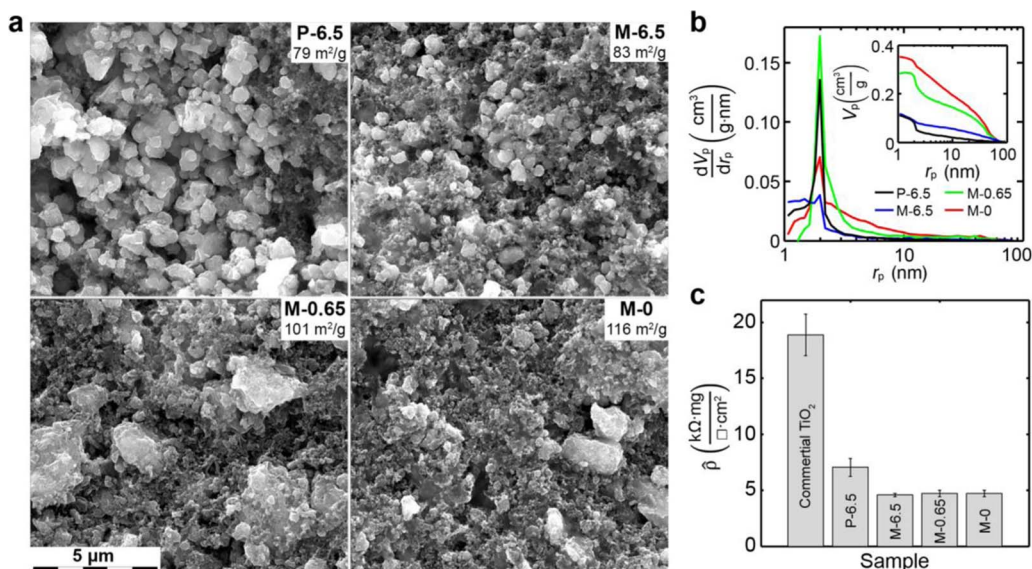


Figure 6. (a) SEM images of the FGS-TiO₂ electrodes; also indicated are the surface areas measured from nitrogen adsorption. (b) Incremental pore volume ($\frac{dV_p}{dr_p}$) as a function of pore width (r_p), as measured from nitrogen desorption isotherms. Inset: Cumulative pore volume (V_p) of the samples, as a function of r_p . (c) Mass-loading specific resistivities, $\hat{\rho}$, measured using a 4-point technique from slurry films that had been cast onto PET and dried.

order to differentiate between material-intrinsic and morphology-related effects, in our analysis of Li^+ transport in the M-samples we focus first on the low mass loading cells before discussing the effect of increased mass loading.

At low mass loadings ($< 1 \text{ mg TiO}_2/\text{cm}^2$) and high specific current ($i = 3.4 \text{ A/g}$), $P_{\text{loss,lith}}$ and $P_{\text{loss,delith}}$ are about the same for all samples, suggesting that at these current densities ($\sim 1.7\text{--}3.4 \text{ mA/cm}^2$) the dissipative losses during cycling are similar in magnitude and we are thus probing the “intrinsic”, i.e., transport-independent, differences in Li^+ capacity between the samples. From M-6.5 to the M-0.65 and M-0 samples, the [SDS] used during processing is reduced to slightly below the cmc and zero, respectively. The resulting absence of bulk-micelle-nucleated TiO_2 implies that the improved high-rate Q_{step} of M-0.65 and M-0 (compared to M-6.5) is due to an enhanced contribution of TiO_2 that is in intimate contact with FGSs (albeit grown via different mechanisms), which may have a greater Li^+ storage capacity than bulk-micelle-nucleated TiO_2 . Furthermore, at the lowest mass loadings, M-0.65 appears to have higher Q_{step} than M-0; this suggests that the presence of adsorbed SDS (but not bulk SDS micelles) is beneficial for templating TiO_2 with enhanced high-rate Li^+ storage capacity on FGSs. It has been reported that adsorbed sulfate ions can orient the growth of anatase TiO_2 such that the [001] axis is perpendicular to the substrate,¹⁶ which could be advantageous in this application as there is also evidence that the diffusion of Li^+ is fastest along that axis.^{54,55}

At the higher electrode mass loadings ($> 1.5 \text{ mg TiO}_2/\text{cm}^2$), the trend in high-rate Q_{step} for the M-samples (M-6.5 $>$ M-0 $>$ M-0.65) is inversely correlated with $P_{\text{loss,lith}}$ and $P_{\text{loss,delith}}$, which reflects the differences in the dissipative losses experienced during cycling. These differences appear to be a result of morphological differences between the samples, which are effected by [SDS]: During the reaction, the [SDS] influences the dispersion state of FGSs (Fig. 5a), which determines the morphology of the FGS- TiO_2 (Fig. 5b) and, in turn, impacts the morphologies of the sample electrodes. At high i , morphology has a measureable impact on electrochemical performance: Q_{step} is inversely correlated with the size of particles/agglomerates (Fig. 6a), which is expected, as longer Li^+ diffusion path lengths within the solid have a negative impact on transport rates.^{8,13–15} Q_{step} is also inversely correlated with the height of the $\frac{dV_p}{dr_p}$ peak at 2 nm (i.e., the population of $\sim 2 \text{ nm}$ pores, Fig. 6b), indicating that depletion of Li^+ in these pores is also detrimental to high-rate performance. While our results do not strictly exclude the possibility that undetected differences in porosity at larger length scales may also impact electrochemical performance, nanoporous electrodes are known to have lower limiting current densities (i.e., the current density above which ion transport in the electrolyte is the limiting step) as compared to fully-dense electrodes.^{56,57} In sum, our results plausibly suggest that differences in Li^+ transport within the FGS- TiO_2 as well as in the electrolyte have a significant impact on the high-rate, high-loading Li^+ storage performance of this material.

Conclusions

The parameters used to process the FGS- TiO_2 nanocomposites clearly affect their Li^+ storage capacities, particularly at high mass loadings and lithiation/de-lithiation rates. We analyzed the impact of FGS- TiO_2 processing by systematically examining the impact of processing parameters, in particular the surfactant concentration, on both the material properties and Li^+ storage capacity of the nanocomposites. Estimating the power loss provides a convenient approach for characterizing the high-rate performance of Li-ion batteries. While FGSs appear to improve e^- transport in the nanocomposites, this does not seem to be the limiting step for the high-rate charging and discharging of thick electrodes. Instead, the SDS concentration used during the processing of FGS- TiO_2 affects the nucleation and growth of TiO_2 as well as the aggregation behavior of FGSs during the reaction, which ultimately determines the structure of FGS- TiO_2 in terms of where TiO_2 forms, particle/agglomerate size, and electrode porosity. Our re-

sults suggest that the transport of Li^+ in these porous electrodes, in the FGS- TiO_2 as well as in the electrolyte, is a major factor in determining the high-rate Li^+ storage capacity. More in-depth studies are necessary to determine the underlying mechanisms for the changes in morphology and the subsequent impact on high-rate performance at high mass loading. As a final note, certain applications demand either high-rate or high-capacity electrodes. Our results demonstrate that customized electrodes can be designed to meet these performance requirements by tuning the processing parameters.

Acknowledgments

This work was supported by the Pacific Northwest National Laboratory (operated for the United States Department of Energy by Battelle) under grant number DE-AC05-76RL01830.

References

- P. Poizot, S. Laruelle, S. Grugeon, L. DuPont, and J. Tarascon, *Nature*, **407**(6803), 496 (2000).
- J.-M. Tarascon and M. Armand, *Nature*, **414**(6861), 359 (2001).
- D. Aurbach, B. Markovsky, I. Weissman, E. Levi, and Y. Ein-Eli, *Electrochim. Acta*, **45**(1), 67 (1999).
- J. Vetter, P. Novak, M. Wagner, C. Veit, K.-C. Möller, J. Besenhard, M. Winter, M. Wohlfahrt-Mehrens, C. Vogler, and A. Hammouche, *J. Power Sources*, **147**(1), 269 (2005).
- M. D. Earle, *Phys. Rev.*, **61**(1-2), 56 (1942).
- O. Johnson, *Phys. Rev.*, **136**(1A), A284 (1964).
- M. Park, X. Zhang, M. Chung, G. B. Less, and A. M. Sastry, *J. Power Sources*, **195**(24), 7904 (2010).
- M. Wagemaker, W. J. Borghols, E. R. van Eck, A. P. Kentgens, G. J. Kearley, and F. M. Mulder, *Chem. Eur. J.*, **13**(7), 2023 (2007).
- L. Kavan, M. Grätzel, J. Rathouský, and A. Zukal, *J. Electrochem. Soc.*, **143**(2), 394 (1996).
- Y.-K. Zhou, L. Cao, F.-B. Zhang, B.-L. He, and H.-L. Li, *J. Electrochem. Soc.*, **150**(9), A1246 (2003).
- A. R. Armstrong, G. Armstrong, J. Canales, and P. G. Bruce, *Angew. Chem. Int. Ed.*, **43**(17), 2286 (2004).
- M. Zúkalova, M. Kalbac, L. Kavan, I. Exnar, and M. Graetzel, *Chem. Mater.*, **17**(5), 1248 (2005).
- Y. S. Hu, L. Kienle, Y. G. Guo, and J. Maier, *Adv. Mater.*, **18**(11), 1421 (2006).
- C. Jiang, I. Honma, T. Kudo, and H. Zhou, *Electrochem. Solid-State Lett.*, **10**(5), A127 (2007).
- Y. G. Guo, Y. S. Hu, W. Sigle, and J. Maier, *Adv. Mater.*, **19**(16), 2087 (2007).
- D. Wang, J. Liu, Q. Huo, Z. Nie, W. Lu, R. E. Williford, and Y.-B. Jiang, *J. Am. Chem. Soc.*, **128**(42), 13670 (2006).
- D. Wang, D. Choi, Z. Yang, V. V. Viswanathan, Z. Nie, C. Wang, Y. Song, J.-G. Zhang, and J. Liu, *Chem. Mater.*, **20**(10), 3435 (2008).
- R. Darkins, M. L. Sushko, J. Liu, and D. M. Duffy, *Langmuir*, **29**(37), 11609 (2013).
- J. Moskon, R. Dominko, M. Gabersek, R. Cerc-Korosec, and J. Jamnik, *J. Electrochem. Soc.*, **153**(10), A1805 (2006).
- S. K. Das, M. Patel, and A. J. Bhattacharyya, *ACS Appl. Mater. Interfaces*, **2**(7), 2091 (2010).
- F.-F. Cao, X.-L. Wu, S. Xin, Y.-G. Guo, and L.-J. Wan, *J. Phys. Chem. C*, **114**(22), 10308 (2010).
- S. K. Das and A. J. Bhattacharyya, *J. Electrochem. Soc.*, **158**(6), A705 (2011).
- S. H. Nam, H.-S. Shim, Y.-S. Kim, M. A. Dar, J. G. Kim, and W. B. Kim, *ACS Appl. Mater. Interfaces*, **2**(7), 2046 (2010).
- I. Moriguchi, R. Hidaka, H. Yamada, T. Kudo, H. Murakami, and N. Nakashima, *Adv. Mater.*, **18**(1), 69 (2006).
- I. Moriguchi, Y. Shono, H. Yamada, and T. Kudo, *J. Phys. Chem. B*, **112**(46), 14560 (2008).
- T. Doi, Y. Miwa, Y. Iriyama, T. Abe, and Z. Ogumi, *J. Phys. Chem. C*, **113**(18), 7719 (2009).
- D. Wang, D. Choi, J. Li, Z. Yang, Z. Nie, R. Kou, D. Hu, C. Wang, L. V. Saraf, J. Zhang, I. A. Aksay, and J. Liu, *ACS Nano*, **3**(4), 907 (2009).
- H. C. Schniepp, J.-L. Li, M. J. McAllister, H. Sai, M. Herrera-Alonso, D. H. Adamson, R. K. Prud'homme, R. Car, D. A. Saville, and I. A. Aksay, *J. Phys. Chem. B*, **110**(17), 8535 (2006).
- M. J. McAllister, J.-L. Li, D. H. Adamson, H. C. Schniepp, A. A. Abdala, J. Liu, M. Herrera-Alonso, R. Car, R. K. Prud'homme, and I. A. Aksay, *Chem. Mater.*, **19**(18), 4396 (2007).
- C. Punckt, F. Muckel, S. Wolff, I. A. Aksay, C. A. Chavarin, G. Bacher, and W. Mertin, *App. Phys. Lett.*, **102**(2), 023114 (2013).
- A. Peigney, C. Laurent, E. Flahaut, R. Bacsá, and A. Rousset, *Carbon*, **39**(4), 507 (2001).
- H. C. Schniepp, K. N. Kudin, J.-L. Li, R. K. Prud'homme, R. Car, D. A. Saville, and I. A. Aksay, *ACS Nano*, **2**(12), 2577 (2008).
- A. G. Hsieh, S. Korkut, C. Punckt, and I. A. Aksay, *Langmuir*, **29**(48), 14831 (2013).
- V. Luca, J. N. Watson, M. Ruschena, and R. B. Knott, *Chem. Mater.*, **18**(5), 1156 (2006).

35. E. Hosono, S. Fujihara, H. Imai, I. Honma, I. Masaki, and H. Zhou, *ACS Nano*, **1**(4), 273 (2007).
36. A. Mitra, A. Bhaumik, and B. K. Paul, *Microporous Mesoporous Mater.*, **109**(1), 66 (2008).
37. A. G. Hsieh, C. Punckt, S. Korkut, and I. A. Aksay, *J. Phys. Chem. B*, **117**(26), 7950 (2013).
38. M. A. Pope, S. Korkut, C. Punckt, and I. A. Aksay, *J. Electrochem. Soc.*, **160**(10), A1653 (2013).
39. D. C. Marcano, D. V. Kosynkin, J. M. Berlin, A. Sinitiskii, Z. Sun, A. Slesarev, L. B. Alemany, W. Lu, and J. M. Tour, *ACS Nano*, **4**(8), 4806 (2010).
40. G. Zhang, B. K. Roy, L. F. Allard, and J. Cho, *J. Am. Chem. Soc.*, **91**(12), 3875 (2008).
41. D. Liao and B. Liao, *Int. J. Chem. React. Eng.*, **5**(1), A24 (2007).
42. M. Corrin and W. D. Harkins, *J. Am. Chem. Soc.*, **69**(3), 683 (1947).
43. A. Chatterjee, S. Moulik, S. Sanyal, B. Mishra, and P. Puri, *J. Phys. Chem. B*, **105**(51), 12823 (2001).
44. T. Marks, S. Trussler, A. Smith, D. Xiong, and J. Dahn, *J. Electrochem. Soc.*, **158**(1), A51 (2011).
45. J. O. Besenhard, *Handbook of Battery Materials*. John Wiley & Sons: (2008).
46. S. Brunauer, P. H. Emmett, and E. Teller, *J. Am. Chem. Soc.*, **60**(2), 309 (1938).
47. D. Dollimore and G. Heal, *J. Appl. Chem.*, **14**(3), 109 (1964).
48. B. Zachau-Christiansen, K. West, T. Jacobsen, and S. Atlung, *Solid State Ionics*, **28**, 1176 (1988).
49. W. Pell and B. Conway, *J. Power Sources*, **63**(2), 255 (1996).
50. T. Christen and M. W. Carlen, *J. Power Sources*, **91**(2), 210 (2000).
51. G. Wu, C. Zhang, T. Miura, S. Asai, and M. Sumita, *J. Appl. Polym. Sci.*, **80**(7), 1063 (2001).
52. C. Punckt, M. A. Pope, and I. A. Aksay, *J. Phys. Chem. C*, **117**(31), 16076 (2013).
53. Y. M. Liu, C. Punckt, M. A. Pope, A. Gelperin, and I. A. Aksay, *ACS Appl. Mater. Interfaces*, **5**(23), 12624 (2013).
54. R. Hengerer, L. Kavan, P. Krtil, and M. Grätzel, *J. Electrochem. Soc.*, **147**(4), 1467 (2000).
55. C. H. Sun, X. H. Yang, J. S. Chen, Z. Li, X. W. Lou, C. Li, S. C. Smith, G. Q. M. Lu, and H. G. Yang, *Chem. Comm.*, **46**(33), 6129 (2010).
56. P. Biesheuvel, Y. Fu, and M. Z. Bazant, *Russ. J. Electrochem.*, **48**(6), 580 (2012).
57. T. R. Ferguson and M. Z. Bazant, *J. Electrochem. Soc.*, **159**(12), A1967 (2012).